

Supplementary Information

Cluster size and composition dependent water deprotonation by free manganese oxide clusters

Sandra M. Lang, Thorsten M. Bernhardt, Denis M. Kiawi, Joost M. Bakker, Robert N. Barnett, and Uzi Landman

S.1 Theoretical Methodology

S.1A Density Functional Theory (DFT) Calculations

The theoretical explorations of the atomic arrangements and electronic structures of the manganese oxide clusters and their complexes were performed with the use of the Born-Oppenheimer spin density-functional theory molecular dynamics (BO-SDFT-MD) method¹ with norm-conserving soft (scalar relativistic for Mn) pseudopotentials² and the generalized gradient approximation (GGA)³ for electronic exchange and correlations. In these calculations we have used a plane-wave basis with a kinetic energy cutoff $E_c = 62$ Ry, which yields convergence. This corresponds to a real-space grid spacing of $0.4 a_0$ (Bohr radius); the real-space grid spacing for the density (and potential) was $0.133 a_0$ corresponding to $E_c = 555$ Ry. In the construction of the Mn pseudopotentials the valence electrons, $3d^5$ and $4s^2$, were characterized by core radii $r_c(s) = 2.35 a_0$ and $r_c(d) = 2.35 a_0$, with the s orbital treated as local. For the oxygen atom pseudopotential the valence $2s^2$ and $2p^4$ electrons were treated with $r_c(s) = r_c(p) = 1.45 a_0$, with the p orbital treated as local.

The BO-SDFT-MD method¹ is particularly suitable for investigations of charged systems since it does not employ a supercell (i.e., no periodic replication of the ionic system is used). In all the calculations the dependence on spin multiplicity has been checked, and the results that we report correspond to the spin multiplicities with the lowest energies. In particular, it is pertinent to note here that in all our calculations the spin-degree of freedom is optimized and used in the computation, unless a particular spin configuration (spin multiplicity) is prescribed. At each step of the calculation the energy levels of the SDFT up-spin and down-spin manifolds in the vicinity of the Fermi level are examined, and the occupation is adjusted such that the spin- Kohn-Sham level with the lower energy eigenvalue gets occupied. For further discussion of spin-isomers see section S.1.B below.

The energy minimization to find the optimal cluster geometry was done with a steepest-descent method. The convergence criteria was that the maximum force magnitude on any particle is less than 0.0005 Hartree/Bohr and that the average over all particles is less than 0.00025 Hartree/Bohr. In some cases BO-SDF-MD simulations of typically a few picosecond duration at 300 K (that is, canonical, constant temperature, simulations, with stochastic thermalization) were used to insure that the resulting optimal configurations were stable; a time-step of 0.25 fs was used in these simulations. For the clusters with adsorbed water longer runs were used to explore configuration space and suggest starting geometries for the minimization. Such ab-initio Born-Oppenheimer MD simulations were also

performed at elevated temperatures, in order to select candidate structural configurations (particularly those found to have lowest potential energies following low-temperature quenches) for the aforementioned steepest-descent optimization. The configurations obtained in these dynamical simulations, together with those constructed by starting from structural configurations of 3D cuboidal or 2D ring and ladder-type motifs, with water molecules attached to the various available sites, form a rich structural pool for (steepest descent) searching for the optimal ground state, and isomeric structures.

S.1B Spin Isomers

Here we comment on the properties of spin isomers for selected bare and water-adsorbed, clusters, discussed in the text (see Figs. 4 and 6); additional information about spin isomers of the $\text{Mn}_4\text{O}_4(\text{H}_2\text{O})_n^+$ ($n= 0, 4$) system can be found in connection with Fig. S9 in the Supplementary Information to Ref. ⁴.

As described in the main text, in all the calculations the dependence on spin multiplicity has been checked, and the results that we report correspond to the spin multiplicities with the lowest energies (global minimum for the ground-state configuration, and local minimum for the isomeric structures); both spin and geometrical isomers are explored. The cluster is initially set up using atomic wave functions, with each iron atom having either five up-spin, or five down-spin, 3d orbitals fully occupied. All possible combinations are tried, including geometry optimization with the orbital occupancy determined by the Fermi distribution function. Evaluation of the energy of the cationic clusters started with removal of an electron from the highest occupied orbital followed by optimization of the cluster geometry and occupancy. We have also tested some cases in which the Mn atoms were not initialized with fully occupied majority spin 3d orbitals, but these failed to yield a lower final energy. In the following we denote the difference between the spin-up and spin-down electrons by $\mu = N_\uparrow - N_\downarrow$.

As noted in the main text for all cases discussed in this paper, the lowest energy isomers of the ionized clusters are found to have high-spin configuration (maximal number of majority spin electrons) regardless of the number of adsorbed water molecules; that is, for $\text{Mn}_4\text{O}_4(\text{H}_2\text{O})_n^+$ $\mu = 19$; in general, for the cationic $\text{Mn}_x\text{O}_x(\text{H}_2\text{O})_n^+$ ($x = 2,3,4$ and $n = 0,1,2,\dots$) clusters that we discussed, the highest $\mu = 5x-1$. The optimal structural optimization of spin-isomers of the above clusters, can be modeled through structural optimization (via total energy minimization) that starts from the lowest energy structure (obtained for maximal μ) and proceeds by minimization of the total energy of the cluster where the 3d spins of selected Mn atoms are flipped (that is become minority-spin electrons); in this way the optimal geometrical and total energy of spin isomers with lower values of μ can be found.

Spin density plots corresponding to certain ground-state structures, and their optimized spin isomers are shown in Figure S1 and Figure S2, together with their relative energies, and the Bader

charges.⁵ In figure S1 we show the results for spin isomers corresponding to geometric isomers of the bare Mn_4O_4^+ clusters, 0-a (ring) , 0-b (cube) in Fig. 4 of the main text, and for the water adsorbed cluster $\text{Mn}_4\text{O}_4(\text{H}_2\text{O})_4^+$ shown as 4-a in Fig. 4. For all the spin isomers we find majority and minority spin distributions that are spatially well localized on the Mn ions. The spin distributions for the $\mu = 19$ distributions are ferromagnetic (all up-spins), whereas the spin distributions for configurations with $\mu = 9$ and $\mu = 1$ are antiferromagnetic for both the ring and cube isomers. Additionally, we find that the total energy of the spin isomers increases as μ decreases. We note that in each case the higher-energy spin isomers are of similar geometry as the maximal μ (lower energy) isomer. The Bader charges show an oxidation state of about 1.5 for the Mn ions in the lowest energy isomers (ring and cube) of Mn_4O_4^+ . On the right side of the figure we show spin distributions for $\text{Mn}_4\text{O}_4(\text{H}_2\text{O})_4^+$, starting (at the top) with the one corresponding to the ground state ($\mu = 19$), which has been displayed in Fig. 4 as isomer 4-a. Higher energy spin isomers (with $\mu = 9$ and 1) are shown below the ground state one, where in each case two ways of obtaining the antiferromagnetic lower μ configuration are shown. The Bader charges for the Mn atoms show two values, corresponding to oxidation states of 1.63 and 1.70; these are somewhat higher than the values found for the bare Mn_4O_4^+ cluster.

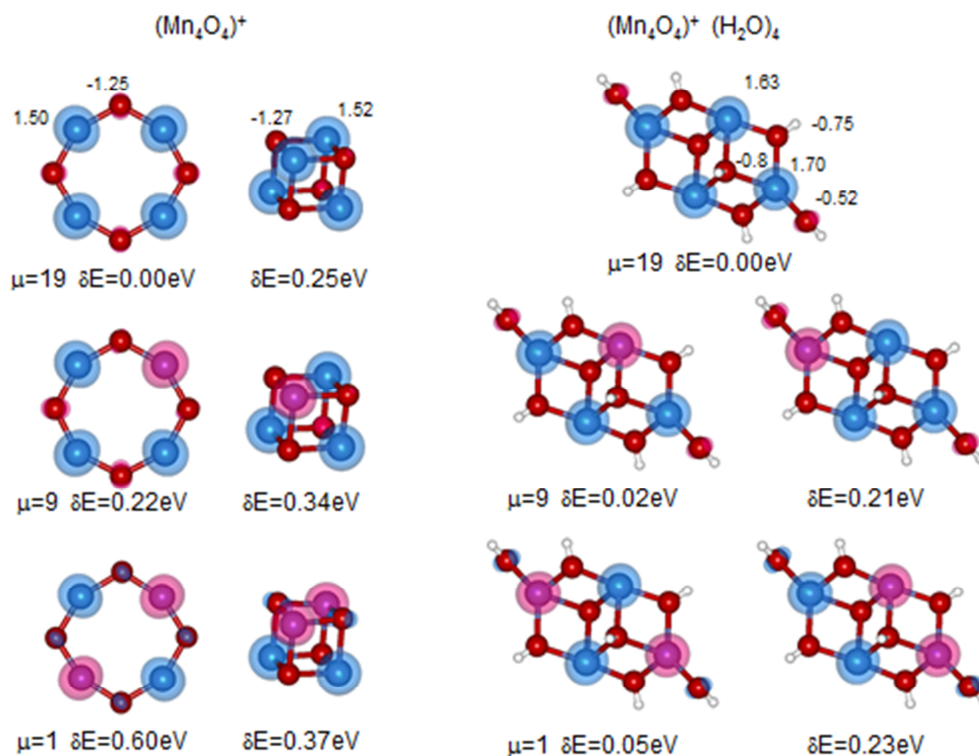


Figure S1. Spatial majority and minority spin density distributions and Bader charges for $\text{Mn}_4\text{O}_4(\text{H}_2\text{O})_n^+$, $n=0$ and 4 . The spin density isosurfaces that we show encompass 80% of the total spin distributions. The majority, up-spin distributions are depicted in blue colour and the minority, down-spin, distributions are shown in pink. The Mn atoms are described by blue spheres, oxygen atoms are represented by smaller red spheres, and hydrogen atoms are displayed as even smaller white spheres. The spin distributions are superimposed on the energy-optimized geometrical structure of the given spin isomer. In each case we indicate the value of $\mu = N_\uparrow - N_\downarrow$ and the energy, δE , relative to the ground-state (lowest-energy) isomer (for which $\delta E = 0$). For Mn_4O_4^+ we show spin distributions for structures corresponding to those shown in Fig. 4 of the text (see Fig. 4 structures 0-a and 0-b), where for both $\mu = 19$ (that is, the ferromagnetic configuration); the higher energy isomers are shown for $\mu = 9$ and 1 . On the right we show spin distributions for $\text{Mn}_4\text{O}_4(\text{H}_2\text{O})_4^+$, starting (at the top) with the one corresponding to the ground state ($\mu = 19$) displayed in Fig. 4 as isomer 4-a. Higher energy spin isomers (with $\mu = 9$ and 1) are shown below the ground state, where in each case two ways of obtaining the antiferromagnetic lower μ configuration are shown. The Bader charges (oxidation states of the Mn atoms) are given for the optimized configurations ($\mu = 19$) for both the bare cluster and with four adsorbed water molecules (dissociatively adsorbed).

Results for spin isomers corresponding to the bare Mn_2O_2^+ cluster (top left in Figure 6 of main text), $\text{Mn}_2\text{O}_2(\text{H}_2\text{O})_4^+$ (marked 4-a in Figure 6), and $\text{Mn}_2\text{O}_2(\text{H}_2\text{O})_5^+$ (marked 5-a in Figure 6), are shown in Figure S2. As in Figure S1, for all the spin isomers we find majority and minority spin distributions that are spatially well localized on the Mn ions. The spin distributions for the $\mu = 9$ distributions are ferromagnetic (all up-spins), whereas the spin distributions for configurations with $\mu = 1$ are antiferromagnetic. The energies of the lower- μ isomers are higher by 0.45 eV, 0.43 eV and 0.36

eV, for the above three cases, respectively. We note that in each case the higher-energy spin isomers are of similar geometry as the maximal μ (lower energy) isomer. The Bader charges show Mn ions with an oxidation state of about 1.6 and 1.8 for the ferromagnetic ground states of the bare and water adsorbed clusters; the Mn ion oxidation states for the higher-energy spin isomers are 1.5 and 1.7 respectively.

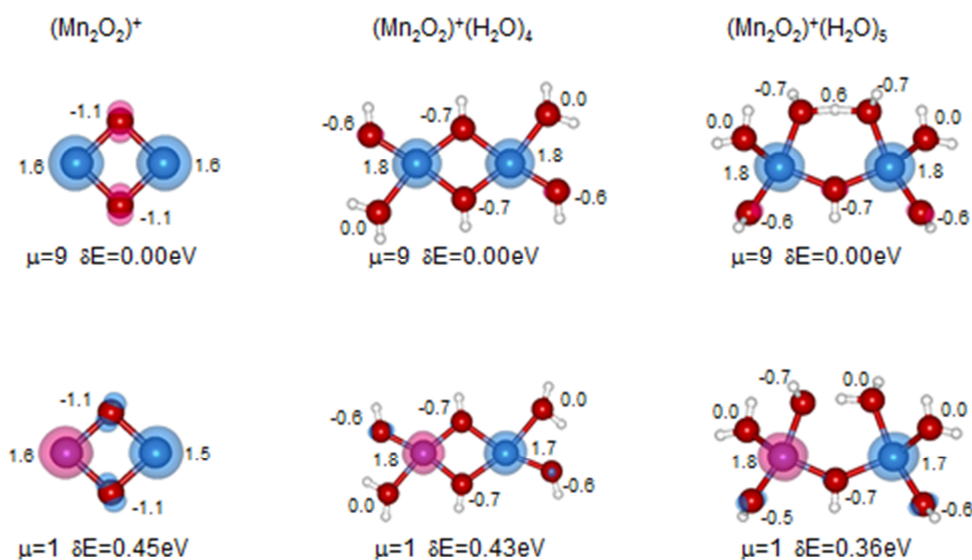


Figure S2. Spatial majority and minority spin density distributions and Bader charges for $\text{Mn}_2\text{O}_2(\text{H}_2\text{O})_n^+$, $n = 0, 4$ and 5 . The spin density isosurfaces that we show encompass 80% of the total spin distributions. The majority, up-spin distributions are depicted in blue colour and the minority, down-spin, distributions are shown in pink. The Mn atoms are described by blue spheres, oxygen atoms are represented by smaller red spheres, and hydrogen atoms are displayed as even smaller white spheres. The spin distributions are superimposed on the energy-optimized geometrical structure of the given spin isomer. In each case we indicate the value of $\mu = N_\uparrow - N_\downarrow$ and the energy, δE , relative to the ground-state (lowest-energy) isomer (for which $\delta E = 0$). For Mn_2O_2^+ we show spin distributions for structures corresponding to the bare ground state shown in the upper left corner of Figure 6 of the main text, with for $\mu = 9$ (that is, a ferromagnetic configuration); for the higher energy (antiferromagnetic) isomer $\mu = 1$. In the middle and on the right we show in the top row spin distributions for the ground state ($\mu = 9$) $\text{Mn}_2\text{O}_2(\text{H}_2\text{O})_4^+$ and $\text{Mn}_2\text{O}_2(\text{H}_2\text{O})_5^+$ clusters (shown in Figure 6 as clusters 4-a and 5-a, respectively). Higher energy spin isomers (with $\mu = 1$) are shown below the ground state ones. The Bader charges are marked in the figure. We note here that in the bare neutral Mn_2O_2 molecule the Bader charge on the Mn atoms (the oxidation state of the metal atoms) is calculated to be somewhat lower (1.16 e).

S2. Vibrational spectra calculations.

In the harmonic approximation the eigenmode frequencies and eigenvectors are determined by direct diagonalization of the dynamical matrix, constructed by finite differencing of the forces at different points near the equilibrium geometry; for each atom two displacements of 0.03 a.u. were performed for each Cartesian direction in the positive and negative directions;⁶ convergence was tested by using a displacement of 0.015 a.u.. From the DFT calculations for these displacements we also evaluate for each of the atoms the effective-charge tensor (the derivative of the dipole of the system with respect to the displacement of the atom), which together with the eigenmode vectors yield the oscillator strengths of the vibrational modes and the IR intensities.⁷ In addition we calculate for each normal mode frequency ν_j the density of states (DOS) projected on each of the atoms $d(i, \nu_j) = \sum_{\alpha} |V_{i\alpha}(j)|^2 \delta(\nu - \nu_j)$ where $\alpha = x, y, z$ and $V_{i\alpha}(j)$ is the i th-atom component in the α th direction of the j th eigenmode vector. pvDOS is the projected vibrational DOS for atoms of type I , $\text{pvDOS}(\nu_j; I) = \sum_i^{(I)} d(i, \nu_j)$ where i is summed over all atoms of type I ; the atom-type index, I , distinguishes in our case, Mn, O (with a distinction between bare O and OH) and H atoms; a large value of $\text{pvDOS}(\nu_j; I)$ indicates a large contribution of atoms of type I to the eigenmode vibration with frequency ν_j .

S3. Bonding of the terminal Oxygen in Mn_2O_3

To elucidate the nature of bonding of a terminal oxygen in $\text{Mn}_x\text{O}_{x+1}$ clusters, the electronic structure has been investigated theoretically using the example of Mn_2O_3 . First we give the adiabatic binding energies - $E_b^{+q} = -E[(\text{Mn}_2\text{O}_3)^{q+}] + E[(\text{Mn}_2\text{O}_2)^{q+}] + E[\text{O}]$ (where $E[X]$ is the total relaxed energy of X), which for $q = 0$ correspond to the neutral cluster and for $q = 1$ to the cationic cluster - obtaining $E_b = 2.92$ eV and $E_b^+ = 1.29$ eV respectively. The geometrical parameters and the Bader charges of $\text{Mn}_2\text{O}_3^{q+}$ ($q = 0, 1$) are given in Figure S3. We observe that the partial negative charge on the oxygen atoms is larger in the neutral molecule, and correspondingly the partial positive charges on the Mn ions (that is, the Mn oxidation states) are larger in the molecular cation. The partial negative charge on the terminal atom (-0.69 e in the neutral molecule and -0.46 e in the cation) is smaller than the negative charges on the bridging oxygens.

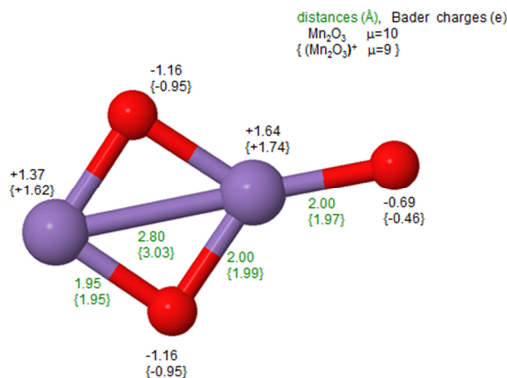


Figure S3. Optimized structure of Mn_2O_3 . Shown is the first-principles energy-minimum structure of Mn_2O_3 ; Mn atoms are represented by purple spheres and the oxygen atoms are displayed as red spheres. Indicated in the figure are the Bader charges⁵ and the interatomic distances (in green) in the neutral {cation} state of the molecule.

The calculated orbital correlation diagram shown in Figure S4, illustrates the orbital scheme for the Mn_2O_2 molecule (left panel) and the way that this cluster combines with the oxygen atom (O, see orbital scheme in the right panel) to form the bound complex Mn_2O_3 (middle panel of Figure S4); note that in these level schemes we specify explicitly the occupancy of the majority (up-spin) and minority (down-spin) levels. For convenience we also recall here that the electronic structure of Mn is $[\text{Ar}] 3d^5 4s^2$, and that of O is $[\text{He}] 2s^2 2p_x^2 2p_y^1 2p_z^1$ (note that both the up and down O $2p_x$ levels are occupied).

The orbital superpositions resulting in formation of the two-dimensional Mn_2O_3 molecule are reflected in the orbital portraits shown in Figure S4. As indicated at the top of Figure S4, for the Mn_2O_2 part (left) we show orbital portraits for those orbitals of Mn_2O_2 that have sufficiently large overlap with the orbitals of Mn_2O_3 , that is: $|\langle \psi_i(\text{Mn}_2\text{O}_2) | \Psi_j(\text{Mn}_2\text{O}_3) \rangle|^2 = 0.1$. Similarly, for the Mn_2O_3 part we select to show those orbitals of Mn_2O_3 whose overlap with the oxygen atom orbitals obey: $|\langle \Psi_i(\text{Mn}_2\text{O}_3) | \phi_j(\text{O}) \rangle|^2 = 0.1$.

The lowest bonding orbital shown in Figure S4 for Mn_2O_3 , is $\Psi_9(\pi, d-p; \text{Mn}_2\text{O}_3)$ which is composed of a π -like superposition of $\psi_{11}(d, \text{Mn}_2\text{O}_2) + \phi_2(2p_x; \text{O})$, where ψ_{11} is of d-character on the Mn ion (from here-on we include the subscripts of the five d-like orbitals originating from the Mn atoms of Mn_2O_2 , as well as those of the 2p orbitals of the O atoms, except when their inclusion adds to the clarity of the discussion); the corresponding antibonding orbital is $\Psi_{14}(\pi^*, d-p; \text{Mn}_2\text{O}_3) \sim \psi_{11}(d; \text{Mn}_2\text{O}_2) - \phi_2(\text{O}, 2p_x)$, having a nodal plane between the Mn_2O_2 and O components. Using the same methodology we find that the σ -bonding Mn_2O_3 orbital $\Psi_{15}(\sigma, d-p; \text{Mn}_2\text{O}_3)$, as well as its σ^* , antibonding $\Psi_{19}(\sigma, d-p; \text{Mn}_2\text{O}_3)$ orbital, are made of $\psi_{13}(d_z^2(\text{Mn}) - \phi_3(2p_3; \text{O}); \text{Mn}_2\text{O}_2) \pm \phi_3(2p_3; \text{O})$. Another contribution to $\Psi_{19}(\sigma, d-p; \text{Mn}_2\text{O}_3)$ comes from the antibonding superposition $\psi_{15}^*(d(\text{Mn}) - \phi(2p_2; \text{O}); \text{Mn}_2\text{O}_2) - \phi(2p_3; \text{O})$, where the Mn_2O_2 part (ψ_{15}^*) is an anti-bonding orbital made of an Mn d-orbital and an O(2p) one. Moving to higher energies we find the Mn_2O_3 π -bonding orbital $\Psi_{17}(\pi, d-p; \text{Mn}_2\text{O}_3)$, and its π^* antibonding conjugate $\Psi_{21}(\pi^*, d-p; \text{Mn}_2\text{O}_3)$ orbitals, made of \pm superpositions of the $\psi_{16}^*(d-p; \text{Mn}_2\text{O}_2)$ - which is a d(Mn)-p(O) antibonding orbital of Mn_2O_2 (similar to the aforementioned ψ_{15}^*) - with the $\phi(2p_4; \text{O})$ p-

orbital of the terminal O atom. Another Mn_2O_3 orbital that mixes into $\Psi_{21}(\pi^*, d-p; \text{Mn}_2\text{O}_3)$, is the anti-bonding $\psi_{18}^*(d-p; \text{Mn}_2\text{O}_2)$ orbital, which is, like ψ_{15}^* and ψ_{16}^* mentioned above, a $d(\text{Mn})-p(\text{O})$ antibonding orbital of Mn_2O_2 .

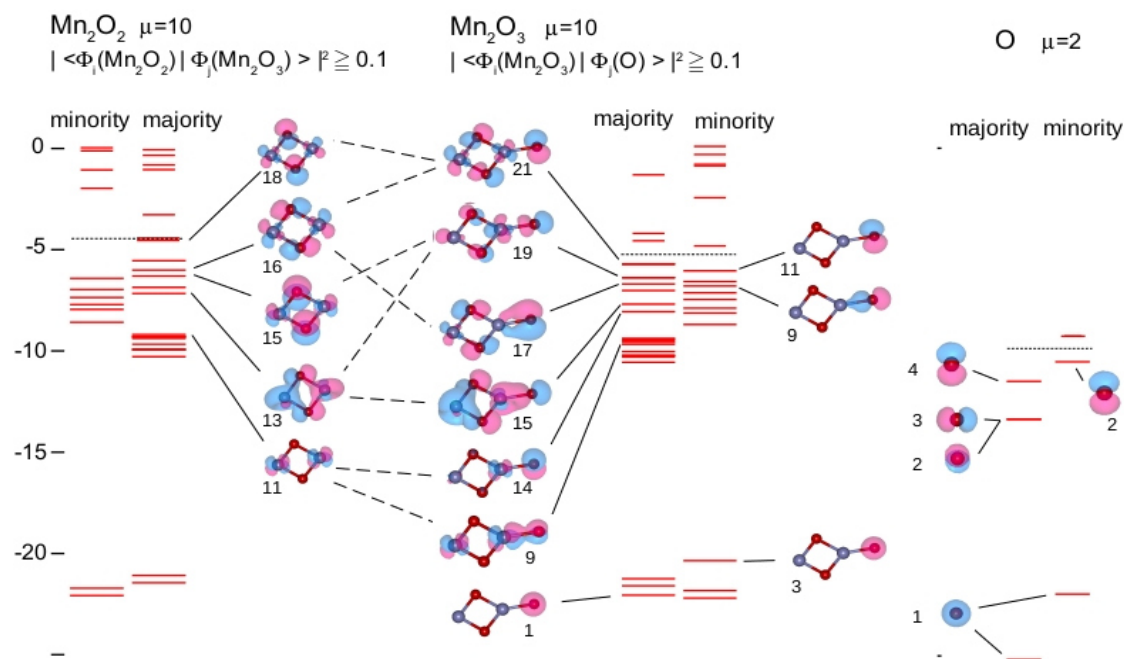


Figure S4. First-principles calculated electronic energy levels and orbital portraits of Mn_2O_2 , Mn_2O_3 and O (from left to right), arranged as a correlation diagram to indicate the bonding (correlation) diagram of Mn_2O_3 . The orbital isosurfaces (encompassing 75%-80 % of the enclosed charge) are displayed in blue and pink, corresponding to positive and negative values, respectively. For each species (Mn_2O_2 , Mn_2O_3 and O, we show the majority (spin-up) and minority (spin-down) levels; the energy values (in eV) are given on the left axis. Orbital portraits for Mn_2O_2 and Mn_2O_3 are shown for those orbitals that obey the conditions displayed at the top of the figure. Also indicated at the top are the values of the difference between the number of majority and minority spins, $\mu = N_\uparrow - N_\downarrow$.

References

- 1 R. N. Barnett; U. Landman. *Phys. Rev. B* 1993, **48**, 2081.
- 2 N. Troullier; J. L. Martins. *Phys. Rev. B* 1991, **43**, 1993.
- 3 J. P. Perdew; K. Burke; M. Ernzerhof. *Phys. Rev. Lett.* 1996, **77**, 3865.
- 4 S. M. Lang; T. M. Bernhardt; D. M. Kiawi; J. M. Bakker; R. N. Barnett; U. Landman. *Angew. Chem. Int. Ed.* 2015, **127**, 15328
- 5 R. F. W. Bader *Atoms in Molecules - A quantum theory*; Oxford University Press: New York, 1990; W. Tang; E. Sanville; G. Henkelman. *J. Phys. Condens. Matter* 2009, **21**, 084204.
- 6 D. Porezag; M. R. Pederson. *Phys. Rev. B* 1996, **54**, 7830.
- 7 P. Giazzoni; S. Baroni. *J. Chem. Phys.* 1994, **100**, 8537.